Ga⁺-focused ion beam damage in n-type Ga₂O₃

Cite as: J. Vac. Sci. Technol. A **40**, 053403 (2022); https://doi.org/10.1116/5.0099892 Submitted: 20 May 2022 • Accepted: 19 July 2022 • Published Online: 10 August 2022

Xinyi Xia, Nahid Sultan Al-Mamun, Daudi Warywoba, et al.













Ga⁺-focused ion beam damage in n-type Ga₂O₃

Cite as: J. Vac. Sci. Technol. A 40, 053403 (2022); doi: 10.1116/5.0099892 Submitted: 20 May 2022 · Accepted: 19 July 2022 ·







Published Online: 10 August 2022

Xinyi Xia, Nahid Sultan Al-Mamun, 2Daudi Warywoba, 3Fan Ren, 1 🕩 Aman Haque, 2 🕩 and S. J. Pearton 4 🕩



AFFILIATIONS

- ¹Department of Chemical Engineering, University of Florida, Gainesville Florida 32611
- ²Department of Mechanical Engineering, Penn State University, University Park, Pennsylvania 16802
- Sengineering, Applied Materials, Penn State University, College Place, DuBois, Pennsylvania 15801

Note: This paper is part of the Special Topic Collection on Gallium Oxide Materials and Devices.

ABSTRACT

Focused Ga+ ion milling of lightly Si-doped, n-type Ga2O3 was performed with 2-30 kV ions at normal incidence and beam currents that were a function of beam voltage, 65 nA for 30 kV, 26 nA for 10 kV, 13 nA for 5 kV, and 7.1 nA for 2 kV, to keep the milling depth constant at 100 nm. Approximate milling rates were 15, 6, 2.75, and $1.5 \,\mu\text{m}^3$ /s for 30, 10, 5, and 2 kV, respectively. The electrical effects of the ion damage were characterized by Schottky barrier height and diode ideality factor on vertical rectifier structures comprising 10 µm epitaxial n-Ga₂O₃ on n⁺ Ga₂O₃ substrates, while the structural damage was imaged by transmission electron microscopy. The reverse bias leakage was largely unaffected even by milling at 30 kV beam energy, while the forward current-voltage characteristics showed significant deterioration at 5 kV, with an increase in the ideality factor from 1.25 to 2.25. The I-V characteristics no longer showed rectification for the 30 kV condition. Subsequent annealing up to 400 °C produced substantial recovery of the I-V characteristics for all beam energies and was sufficient to restore the initial ideality factor completely for beam energies up to 5 kV. Even the 30 kV-exposed rectifiers showed a recovery of the ideality factor to 1.8. The surface morphology of the ion-milled Ga₂O₃ was smooth even at 30 kV ion energy, with no evidence for preferential sputtering of the oxygen. The surface region was not amorphized by extended ion milling (35 min) at 5 kV with the samples held at 25 °C, as determined by electron diffraction patterns, and significant recovery of the lattice order was observed after annealing at 400 °C.

Published under an exclusive license by the AVS. https://doi.org/10.1116/5.0099892

I. INTRODUCTION

Focused ion milling of semiconductors is commonly used for device mesa patterning, localized implantation, sample preparation for transmission electron microscopy, and potentially for future microcircuit editing.^{1–5} Focused ion beams (FIBs) can also be used to image the sample via secondary electrons or ions during or after localized milling, but they are more typically used as a milling technique to pattern the semiconductor surface with micrometer size features. This technique is now being applied to the ultrawide bandgap semiconductor Ga₂O₃, which is attracting interest for power electronics and solar-blind UV detectors. 6-10 Kalanov et al. 11 reported that the main secondary ions for the ion beam sputtering of Ga₂O₃ using O₂⁺ and Ar⁺ ions are Ga⁺, O⁺, and O₂⁺. Little is known about the effect of FIB on the electrical and structural properties of Ga₂O₃, which must be rectified as this technique is integrated into process schemes for devices or TEM sample preparation. For example, the depth, severity, and thermal stability of the ion-induced damage as a function of beam energy are important to understand. There have been a number of studies of ion beam damage in Ga2O3 for ion implantation applications at hundreds of keV energy^{12–19} and several for lower energies.^{20,21}

An issue that has arisen previously with other compound semiconductors is how well the standard range and damage simulation codes accurately correlate with experimental data.²²⁻²⁹ It has been commonly observed that the depth to which damage is observed experimentally is much larger than the projected range of the ions, and this has been ascribed to a rapid diffusion of defects created by the beam. $^{\rm 30-32}$ The commonly used binary collision Monto Carlo simulation programs include static and dynamic TRIM for sequential and parallel computer (SDTrimSP), TRIDYN, and stopping and range of ions in matter (SRIM)²²⁻²⁹. The latter is the most commonly used code due to its extensive database on compound target materials and electronic energy loss data. TRIDYN and SDTrimSP are similar to SRIM but use the krypton-carbon interaction potential.²⁶⁻²⁹ While it is known that the angular distributions are generally more accurate in

⁴Department of Material Science and Engineering, University of Florida, Gainesville Florida 32611

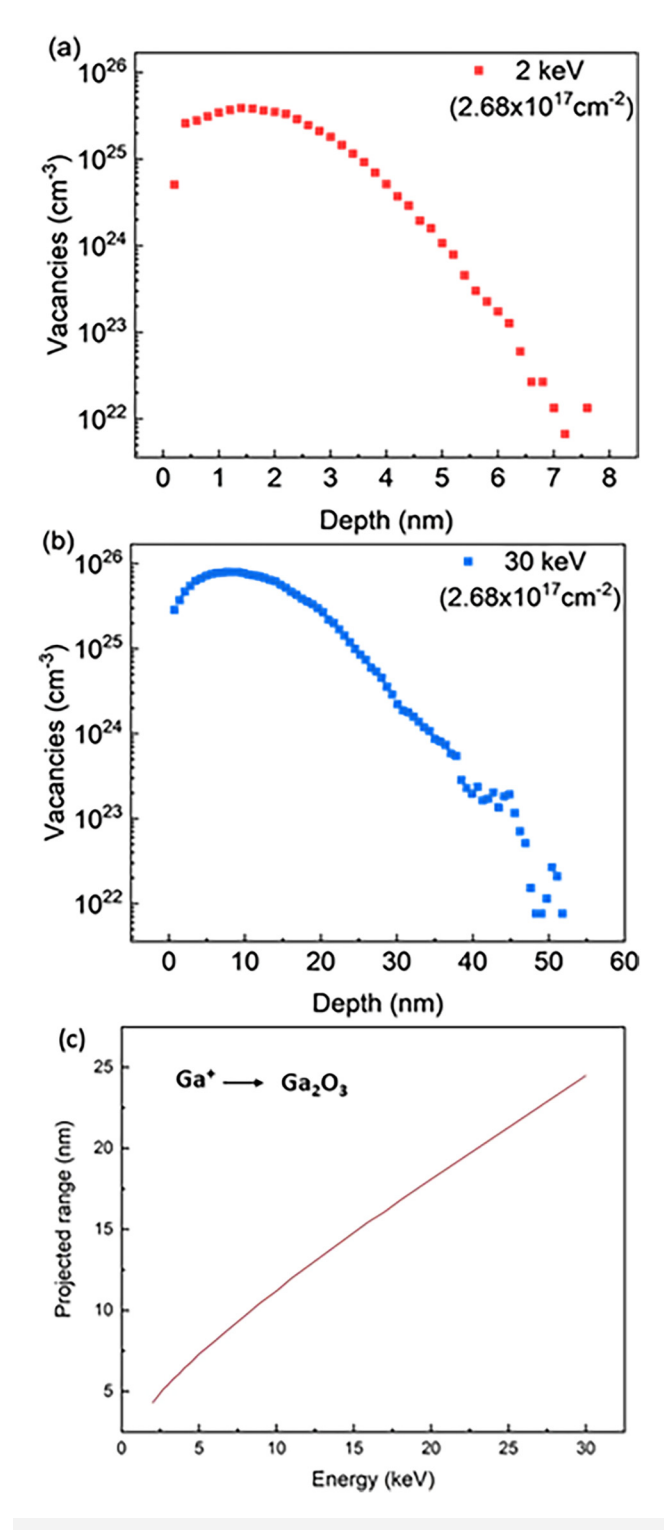


FIG. 1. SRIM simulations of vacancy distributions created by the ${\sf Ga}^+$ ion in ${\sf Ga}_2{\sf O}_3$ at (a) 2, (b) 30, and (c) the projected range as a function of energy. Points for the 2 kV condition are in red, while those for 30 kV are in blue.

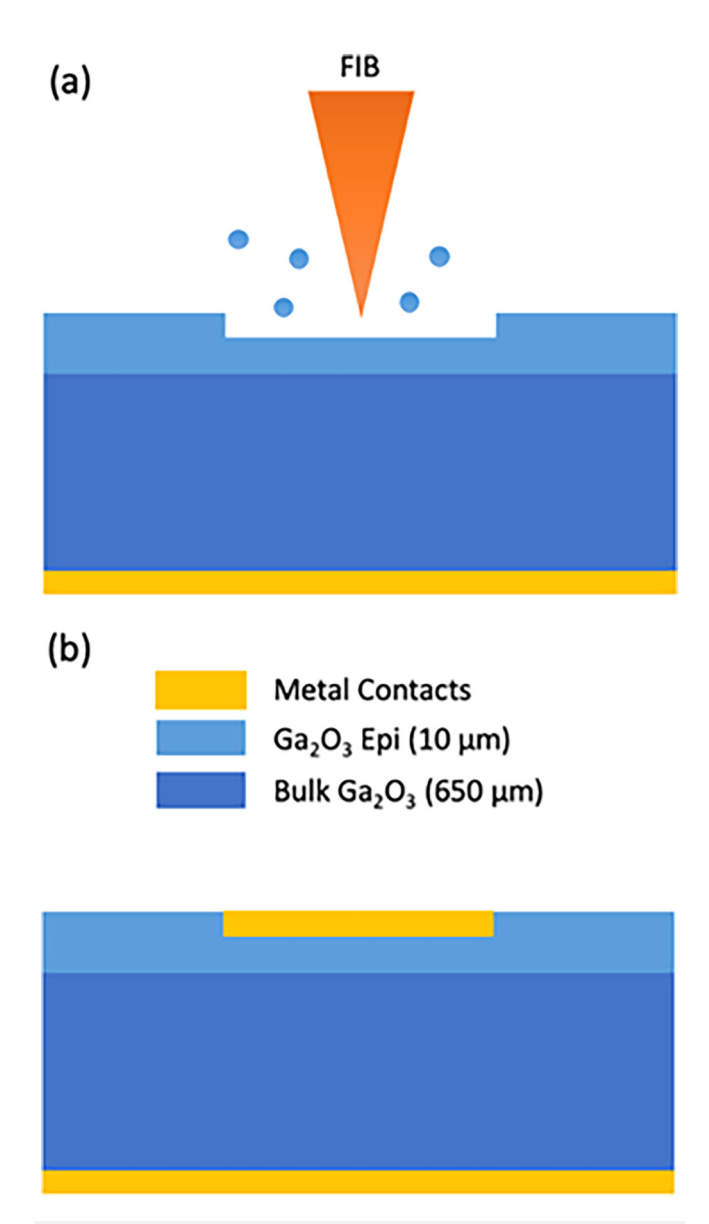


FIG. 2. Schematic of sample preparation. (a) After exposure to the Ga⁺ ion beam, (b) a front-side Schottky contact was deposited for allowing a measurement of I–V characteristics. The epilayer (at top) is light blue, the substrate (center of structure) is darker blue, and the back of the metal contact(bottom of structure) is yellow.

the latter two codes, SRIM is commonly used as a first approximation to get the projected range of the ions. $^{22-24}$

In this paper, we report on the effect of Ga⁺ ion beam energy on changes to the near surface of Ga₂O₃. We measure these changes by using Schottky contacts evaporated onto the ion beam-exposed surface without additional surface treatments, in order to capture the condition of the as-damaged surface. Postbeam annealing is also investigated to establish the thermal stability of the ion-induced damage.

II. EXPERIMENT

The range of the Ga+ ions was simulated by SRIM. Figure 1 shows the SRIM simulated vacancy distributions for the limits of ion energy used here, namely, (a) 2 and (b) 30 kV, along with the projected range (c). As discussed earlier, these can be considered as a lower limit for the depth of the damage induced by the beam. The dose was 2.68×1017 ions cm⁻² for the 2 kV energy, calculated from the milled volume $(55 \times 55 \times 0.1 = 302.5 \,\mu\text{m}^3)$. Then, the milling time to get the dose at each energy was calculated from this volume times the milling rate. Note that that each atom will be displaced many times from its regular position, so if all vacancies survive, the sample surface will be amorphous. However, there is a simultaneous sputter removal of the surface and an efficient dynamic annealing of vacancies by recombination. It is also important to note that in the case of high dose ion irradiation, when the thickness of the etched by ions layer is greater than the projected range ΔRp , the Gaussian-like distributions of implanted ions and created defects become boxlike.³⁰ So, the implanted atom concentration in the vicinity of the surface can be roughly estimated as N/S, where N is the host atom concentration and S is the sputtering coefficient.

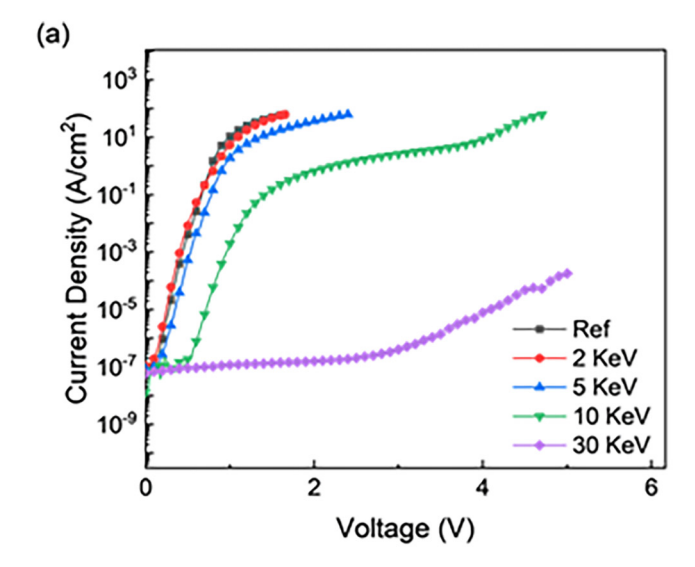
We used vertical rectifier structures as our platform for investigating the FIB-induced damage. These consisted of a $10\,\mu m$ -thick, lightly Si doped epitaxial layer grown by halide vapor phase epitaxy (HVPE) with carrier concentration $2\times 10^{16}~cm^{-3}$, grown on a (001) surface orientation Sn-doped $\beta\text{-Ga}_2\text{O}_3$ single crystal (Novel Crystal Technology, Japan). A full area Ti/Au backside Ohmic contact was formed by e-beam evaporation and was annealed at 550 °C for

100 μm

FIG. 3. Optical microscope image of the front contact geometry. The metal contacts (squares and circles) appear gold, while the region outside the device area is brown.

1 min under N_2 ambient. This was done to avoid the very large changes in conductivity that can be induced by annealing under O_2 atmospheres.

The samples were processed as shown schematically in Fig. 2. The samples with Ohmic contacts in place, but prior to evaporation of the front contact, were exposed to focused Ga^+ ions at normal incidence, energies of 2–30 kV, and beam currents that were a function of beam voltage, 65 nA for 30 kV, 26 nA for 10 kV, 13 nA for 5 kV, and 7.1 nA for 2 kV, to keep the milling depth constant at



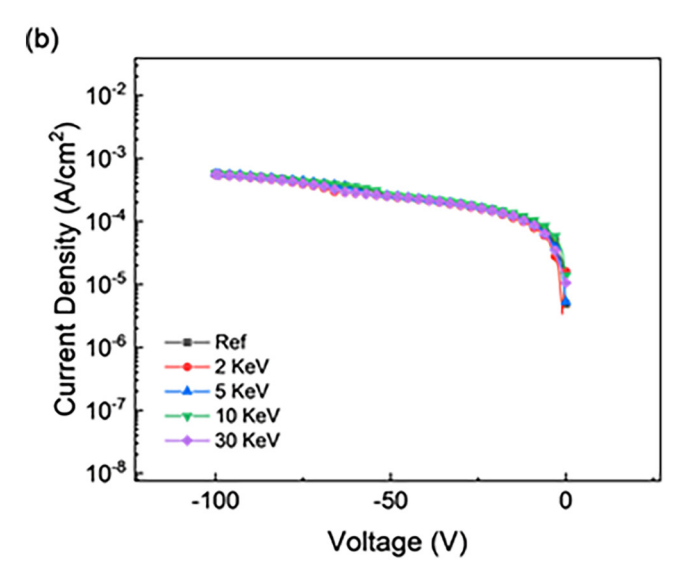


FIG. 4. (a) Forward and (b) reverse I–V characteristics from 55 μm circular contacts for different energy Ga⁺ ion beam exposures. The points for 2 kV are shown in red, for 5 kV in blue, for 10 kV in green, and for 30 kV in purple in the forward I-Vs, the current gets lower as beam energy increases.

TABLE I. Summary of electrical data from ion beam-exposed samples that were subsequently annealed at different temperatures. The samples exposed to 30 keV beams no longer showed rectifying behavior until they were annealed at 400 °C.

Sample	N	Φ_B (eV)	$R_{\rm on}~({\rm m}\Omega~{\rm cm}2)$
Control-as-is	1.50	0.88	3.0
Control-300 °C	1.32	1.01	2.9
Control-350 °C	1.77	1.01	2.7
Control-400 °C	1.47	1.12	2.9
2 keV-as-is	1.94	0.77	3.0
2 keV-300 °C	1.32	1.10	2.9
2 keV-350 °C	1.54	1.18	2.8
2 keV-400 °C	1.55	1.18	3.0
5 KeV-as-is	2.25	0.83	3.1
5 KeV-300 °C	1.35	0.99	3.0
5 keV-350 °C	1.69	1.14	2.4
5 keV-400 °C	1.51	1.10	2.6
10 keV-as-is	3.88	0.74	392.8
10 keV-300 °C	1.83	1.05	17.0
10 keV-350 °C	1.69	1.14	3.3
10 keV-400 °C	2.03	1.13	2.0
30 keV-as-is	_	_	_
30 keV-300 °C	_	_	_
30 keV-350 °C	_	_	_
30 keV-400 °C	1.49	1.16	2.6

100 nm. The approximate milling rates for Ga₂O₃ were 15, 6, 2.75, and $1.5 \,\mu\text{m}^3$ /s for 30, 10, 5, and 2 kV, respectively. After the exposure to the Ga beam, a 20/80 nm Ni/Au Schottky contact was deposited with e-beam evaporation through a shadow mask. An optical microscope image of the contact pattern is shown in Fig. 3. We measured either the $400 \times 400 \,\mu m$ squares or the circular 55 µm diameter devices to check differences due to surface recombination, which would have a larger effect on the latter. Within experimental error, we saw no differences in current density at a given voltage, so this was not a factor. However, we did note macroscopic variations in low-bias currents from devices taken from different areas of the patterned wafer. Thus, for all sets of different energy exposures, we used devices from the same local area on the wafer. In this case, variations were within 10%. The current-voltage (I-V) characteristics were recorded with a Tektronix 370-A curve tracer, 371-B curve tracer, and Agilent 4156C. Given the doping in the epilayers, it is expected that thermionic emission dominates as the main current conduction mechanisms. In this case, the current density J is given by

$$J = A^* T^2 \exp(-e(\Phi_B - \Delta \Phi)/k_B T) \exp[(eV/nk_B T) - 1],$$

where A^* is the Richardson constant, T is the absolute temperature, e is the electronic charge, Φ_B is the barrier height, $\Delta\Phi$ is the image force barrier lowering, k_B is Boltzmann's constant, and n is the ideality factor. We used the changes in extracted barrier height and ideality factor as a result of ion beam exposure as a quantitative measure of the magnitude of the ion-induced damage for the beam energy, along with the on-state resistance $(R_{\text{on-sp}})$ obtained from

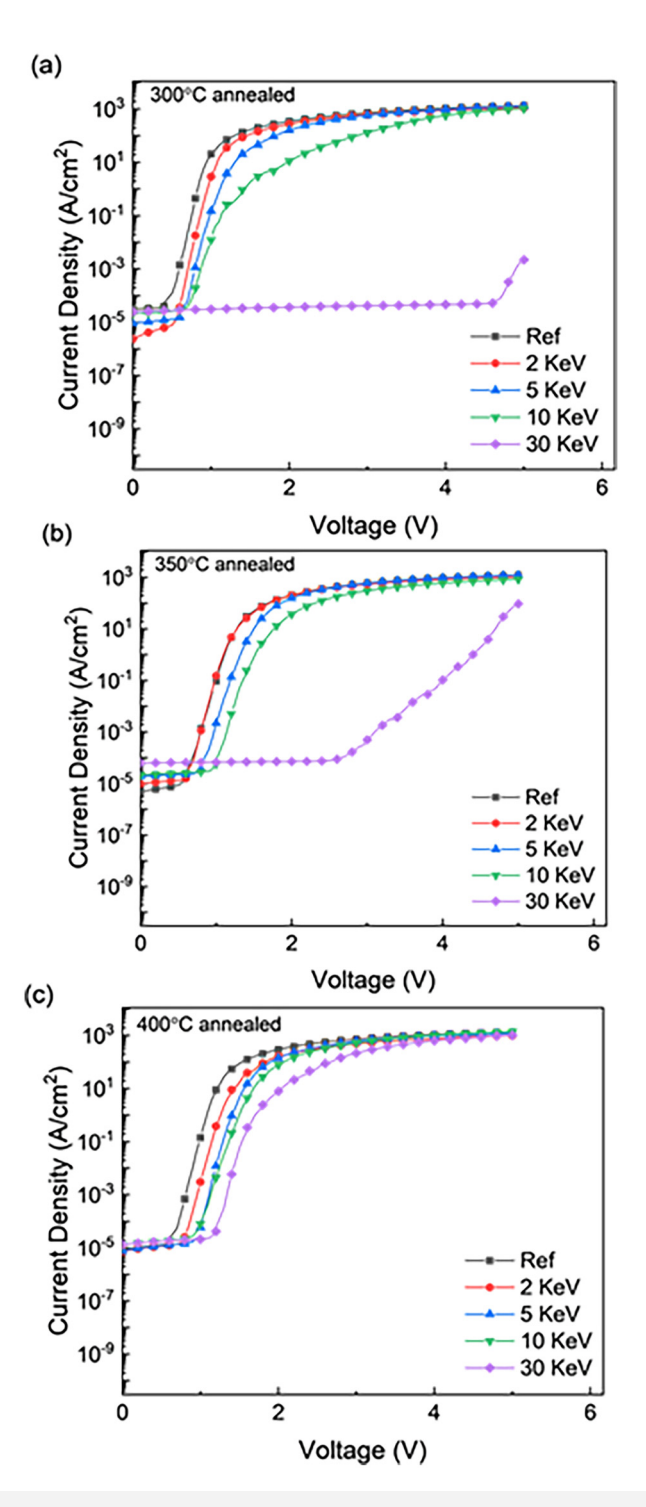


FIG. 5. Forward I–V characteristics from $55\,\mu\mathrm{m}$ circular contacts for different energy Ga $^+$ ion beam exposures after subsequent annealing at (a) 300, (b) 350, or (c) 400 °C. The points for 2 kV are shown in red, for 5 kV in blue, for 10 kV in green, and for 30 kV in purple. In all plots, the current decreases with increasing beam energy.

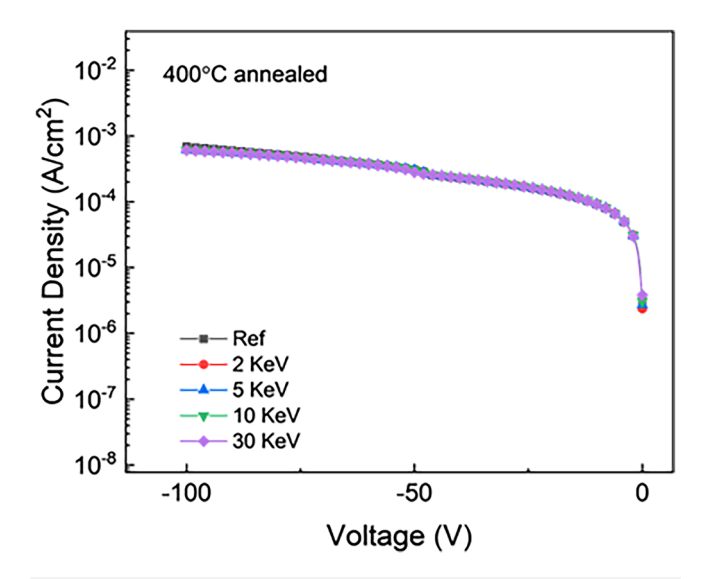


FIG. 6. Reverse I–V characteristics from $55\,\mu\mathrm{m}$ circular contacts for different energy Ga+ ion beam exposures after subsequent annealing at 400 °C. The points for 2 kV are shown in red, for 5 kV in blue, for 10 kV in green, and for 30 kV in purple. There was no significant difference in current between the different energies.

the slope of the forward I-V characteristic. In a standard device design, increasing the thickness, L_N , or decreasing the doping, N_d , of an n-drift region increases the on-resistance, as given by $R_{\text{on-sp}} = \frac{L_N}{e\mu_n N_d}$,

where e^{i} is the electronic charge and μ_n is the electron mobility. The relationship between on-resistance and blocking voltage is

$$R_{\text{on-sp}} = \frac{4V_B^2}{\varepsilon_s \mu_n E_s^3},$$

where ε_s is the dielectric constant of the semiconductor and E_c is the critical electric field. Note that the introduction of trap states related to the ion beam damage is likely to reduce N_d , and conversely, subsequent annealing can restore a part of this carrier concentration.

Annealing after focused ion beam exposures were done for 60 s in N₂ atmospheres at temperatures of 300, 350, or 400 °C.

The samples were also examined by cross-sectional TEM to examine crystal quality near the interface. The electron transparent cross-sectional lamellae of ~100- nm thickness were prepared using the FEI Helios Nanolab 660 dual-beam-focused ion beam. The bright field TEM images and nanodiffraction patterns were obtained with the FEI Talos F200X scanning/transmission electron microscope (S/TEM) using a field emission gun at 200 kV of acceleration voltage.

III. RESULTS AND DISCUSSION

Figure 4(a) shows the forward I-V characteristics from rectifiers exposed to different Ga+ ion beam energies. Compared with the

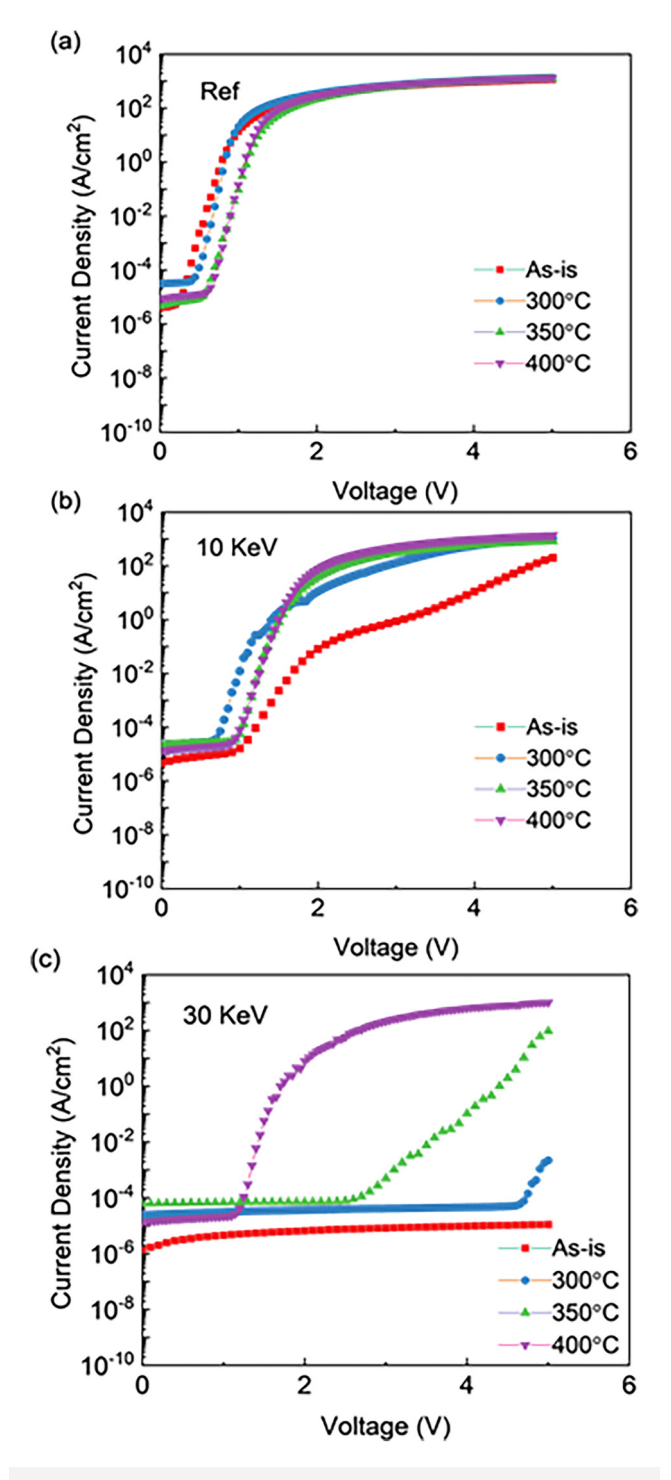


FIG. 7. Forward I–V characteristics from $55\,\mu\mathrm{m}$ circular contacts for (a) unexposed, (b) 10, or (c) 30 keV-exposed diodes before and after subsequent annealing at temperatures of 300, 350, or 400 °C. The points for as-grown are shown in red, for 300 °C in blue, for 350 °C in green, and for 400 °C in purple. The current increases in all cases with annealing temperature.

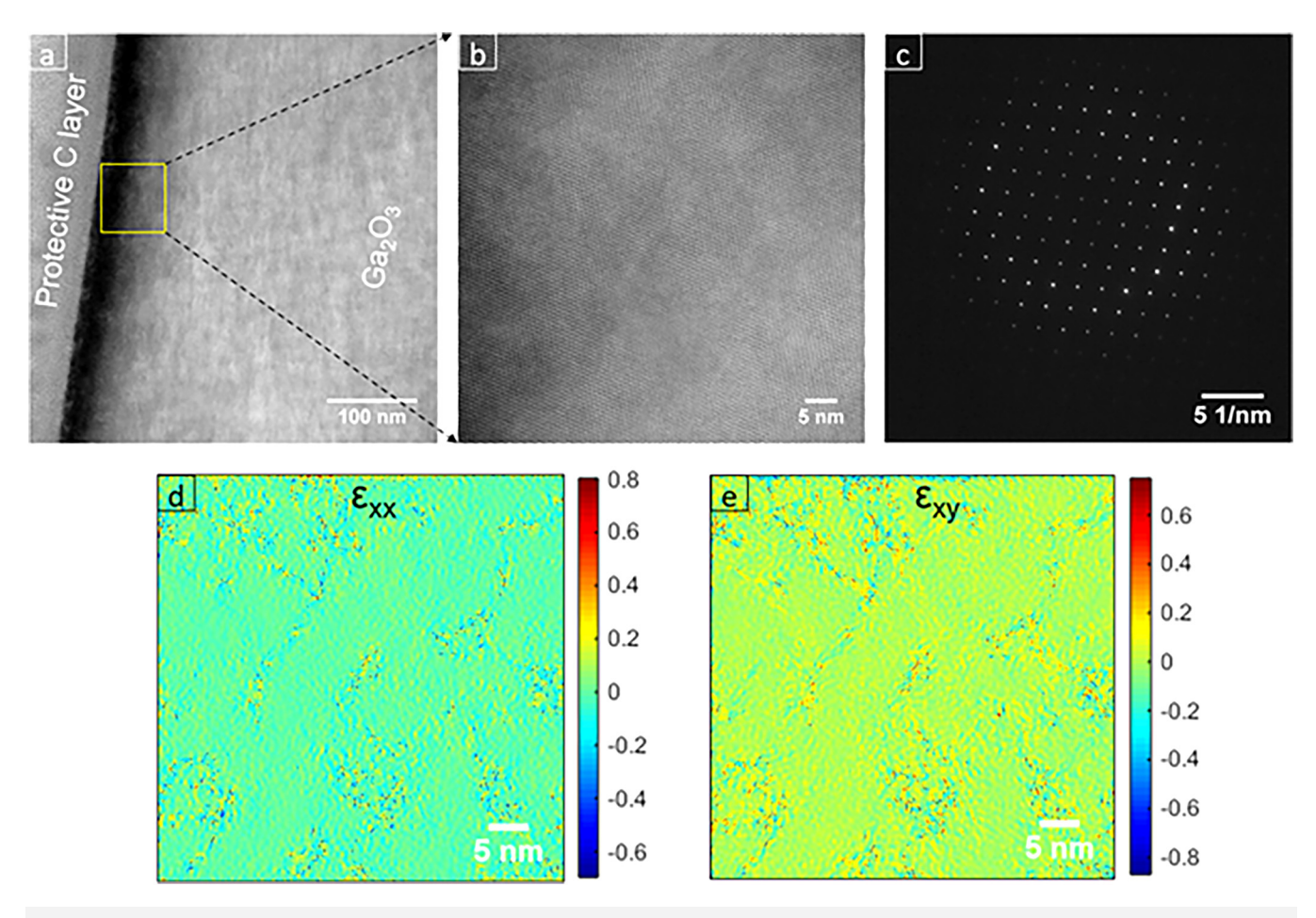


FIG. 8. TEM analysis of a 2 kV Ga⁺ ion-exposed sample (a) bright field cross-sectional image, (b) HRTEM image, (c) nanodiffraction pattern, (d) normal strain, and (e) shear strain field associated with dislocations. The scale on the bottom figure shows increasing values from the minimum in blue to the maximum in red. The false-color images are in green, indicating values just above zero. The values are slightly higher in the plot at left.

reference device, Ga^+ ion beam exposure leads to progressively larger amounts of degradation in the forward current with increasing energy. The Φ_B , N, and R_{on} values before and after ion beam exposure are given in Table I. Note that the extracted barrier height includes the barrier image force lowering, $\Delta\Phi$. More discussions of the magnitude and effects of this parameter are given elsewhere, where it is also established that thermionic emission is the dominant current conduction mechanism in β -Ga₂O₃ Schottky diodes at the doping level used here. The focus in this work is to simply use the extracted barrier height as an indicator of damage introduction or repair. For this reason, we do not include also the threshold voltage or built-in potential that is clearly different after annealing or after irradiation. Richardson's constant was calculated to be in the range of $28.8-41.8~\mathrm{A/cm^2}~\mathrm{K^2}$ for the diodes still exhibiting ideality factors < 2, which again are consistent with literature values.

Even for a 5 kV exposure, the ideality factor increases beyond 2, which is indicative of a strong contribution from other conduction mechanisms like defect-assisted tunneling and recombination.

For 30 keV beam exposure, the rectifier no longer has a recognizable forward I-V characteristic. In sharp contrast, the reverse I-V characteristics, shown in Fig. 4(b), exhibit no significant change for any of the beam energies. This may be due to the fact that the reverse current is averaged over contributions from the entire epitaxial layer thickness, and this is less affected by the presence of a thin and almost damaged region near the surface than if the damage were created throughout the entire layer thickness. This emphasizes the value of using the forward characteristics from rectifiers as a sensitive measure of near-surface disorder. In addition, to place the results in context, Ni Schottky contacts on Ga₂O₃ typically display barrier heights in the range of 0.84-1.54 eV when determined by I-V measurements, with on-state resistance $4.09-10.5 \,\mathrm{m}\Omega \,\mathrm{cm}^{2.34-36}$ These large variations reflect the influence of surface quality, deposition method, presence of additional conduction methods and orientation, among others. Our values fall within these ranges but emphasize that measurements must be made on a consistent set of samples.

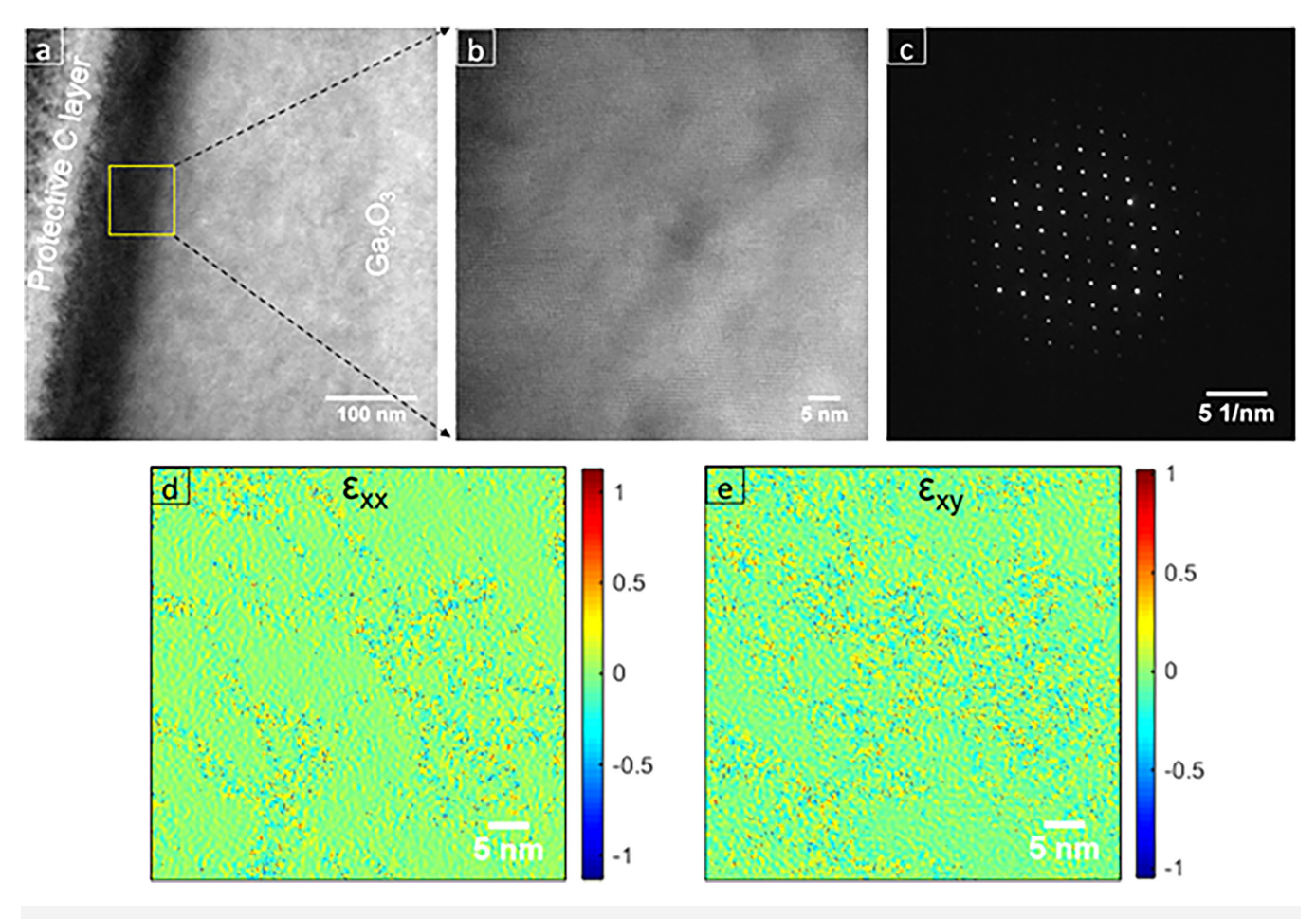


FIG. 9. TEM analysis of a 30 kV Ga⁺ ion-exposed sample (a) bright field cross-sectional image, (b) HRTEM image, (c) nanodiffraction pattern, (d) normal strain, and (e) shear strain field associated with dislocations. The scale on the bottom figure shows increasing values from the minimum in blue to the maximum in red. The false-color images are in green, indicating values just above zero. The values are basically the same in both plots.

The effect of post ion beam exposure annealing on the forward I–V characteristics for different ion energies is shown in Fig. 5 for annealing temperatures in the range of 300–400 °C. The highest temperature brings significant recovery in the forward current, even for the 30 kV exposure. As shown in Table I, lower temperature anneals do not bring much restoration of the current for the 30 kV case. We could not anneal at higher temperatures due to the onset of contact degradation. Once again, the reverse I–V characteristics did not show any significant change with annealing, as seen in Fig. 6.

Figure 7 shows the changes in forward I–V characteristics in more detail before (a) and after (b) the 10 and (c) 30 kV exposures. Annealing the control sample leads to some changes in current as the barrier height is affected, while the extent of recovery for the ion beam-exposed samples depends on the beam energy. The recovery is due to removal of point defects that induce the tunneling and recombination in the near-surface region. Previous work has shown

that the proton and electron radiation-induced damage in Ga_2O_3 also reveals a significant recovery stage around 400 °C. ^{37,38}

The bright field cross-sectional TEM images of the $2 \, \text{kV}$, $30 \, \text{kV}$ Ga⁺ ion-exposed samples and the annealed $30 \, \text{kV}$ ion-exposed samples are shown in Figs. 8(a)-10(a), respectively. The HRTEM images, shown in Figs. 8(b)-10(b), and the nanodiffraction patterns shown in Figs. 8(c)-10(c) obtained at the near-surface regions confirm that no amorphization has occurred due to Ga⁺ ion milling. The atomic strain mapping was performed on the HRTEM images using the geometric phase analysis (GPA) technique described previously³⁹, and the corresponding normal strain in the x direction (ε_{xx}) and shear strain in the x-y plane (ε_{xy}) are presented in Figs. 8(c) and 8(d)-10(c) and 10(d), respectively. The location of individual dislocations on the samples can be identified by the relative strain values. A significant increase in dislocations is observed when the ion beam energy is increased from $2 \, \text{kV}$ [Figs. 8(c) and 8(d)] to $30 \, \text{kV}$ [Figs. 9(c) and 9(d)]. However, a remarkable

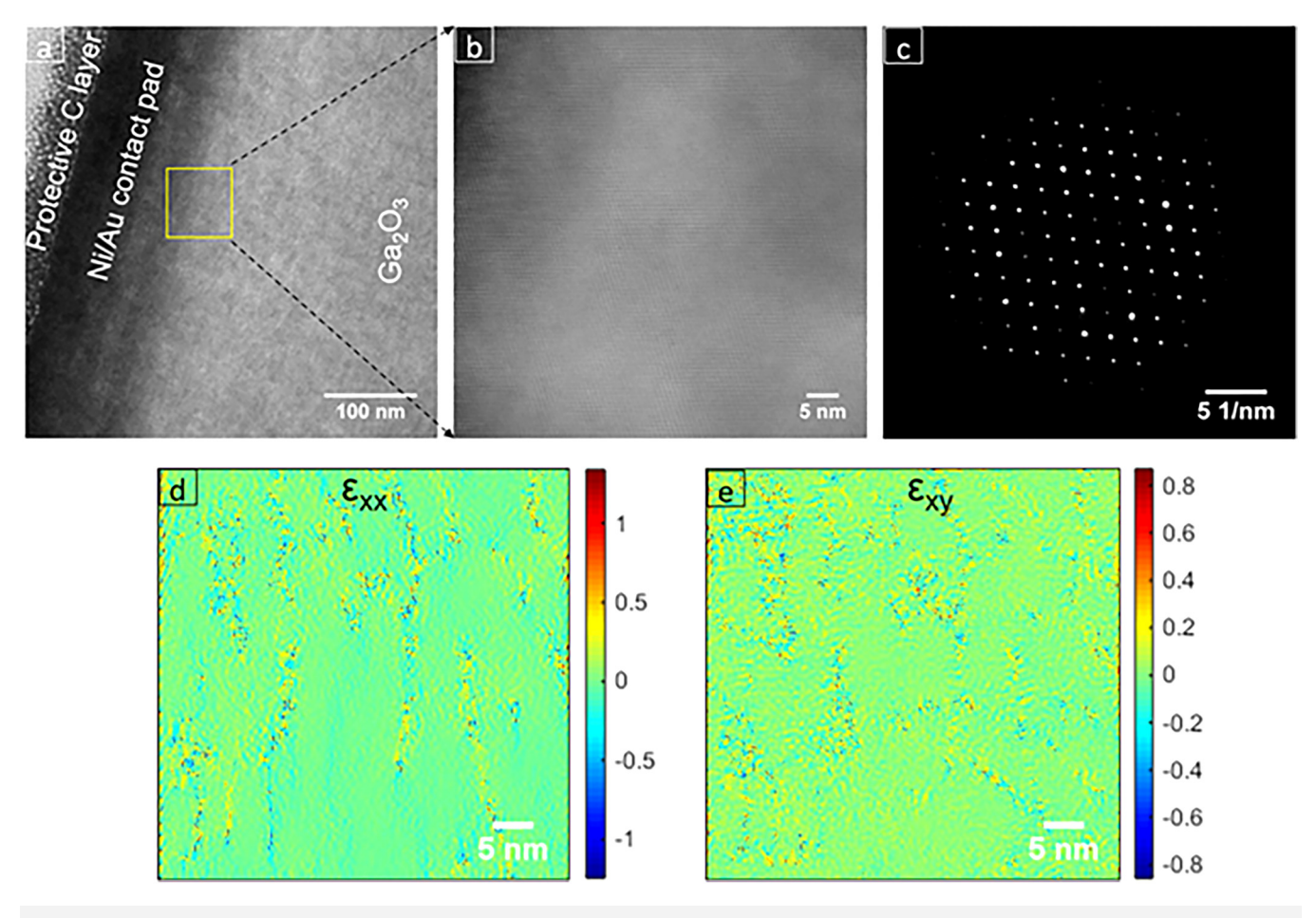


FIG. 10. TEM analysis of a 30 kV Ga⁺ ion-exposed sample after annealing at 400 °C (a) bright field cross-sectional image, (b) HRTEM image, (c) nanodiffraction pattern, (d) normal strain, and (e) shear strain field associated with dislocations. The scale on the bottom figure shows increasing values from the minimum in blue to the maximum in red. The false-color images are in green, indicating values just above zero. The values are basically the same in both plots.

reduction in dislocations can be observed in the $30\,\mathrm{kV}$ ion-exposed sample after annealing at $400\,\mathrm{^{\circ}C}$ [Figs. 10(c) and 10(d)].

Finally, we note that the surface morphology remained smooth under all our conditions, and we did not observe any preferential loss of oxygen and any formation of Ga droplets. We have seen such metal droplet formation previously on InP³⁰ and GaN under very high ion energy conditions, >50 kV.

IV. SUMMARY AND CONCLUSIONS

 \mbox{Ga}^{+} ion beam damage was investigated in $\mbox{Ga}_{2}O_{3}$ as a function of ion energy (2–30 keV) and postexposure annealing. The electrical characteristics of Schottky diodes fabricated on the ion beam-exposed surfaces were much more sensitive to damage in the forward bias direction, with reverse bias leakage current being largely unaffected. The ideality factor and barrier height were

degraded even after beam exposures as $5\,\mathrm{kV}$, but annealing at $400\,^\circ\mathrm{C}$ brought significant recovery for all but the highest beam energies. The surface is not amorphized under any of the conditions employed in our study.

It is important to note that while we have used ion energy as the main parameter of irradiation, a change in the ion energy also leads to a change in the number of defects generated by an ion. This density of defects determines the amount of degradation of the Schottky diodes. However, since the sputtering coefficient increases with increasing energy, an increase in the latter leads to a decrease in the number of ions per unit surface required to etch off a given thickness of Ga_2O_3 . Thus, the interplay of all these factors determines the severity of degradation. In future studies, we plan to examine the use of lower-energy beams to repair damage created at higher energies, since it is the net effect of initial damage created minus the amount subsequently repaired that matters for the device performance.



ACKNOWLEDGMENTS

This work was funded by the Defense Threat Reduction Agency (DTRA) as part of the Interaction of Ionizing Radiation with Matter University Research Alliance (IIRM-URA) under Contract No. HDTRA1-20-2-0002. The work at UF was also supported by NSF No. DMR 1856662 (James Edgar). The work at PSU was also supported by NSF No. ECCS 2015795. The content of the information does not necessarily reflect the position or the policy of the federal government, and no official endorsement should be inferred.

AUTHOR DECLARATIONS

Conflicts of Interest

The authors have no conflicts to disclose.

Author Contributions

Xinyi Xia: Data curation (equal); Visualization (equal). Nahid Sultan Al-Mamun: Data curation (equal); Writing – review & editing (equal). Daudi Warywoba: Conceptualization (equal); Data curation (equal). Fan Ren: Conceptualization (equal); Writing – original draft (equal). Aman Haque: Conceptualization (equal); Data curation (equal); Writing – original draft (equal); Writing – review & editing (equal). S. J. Pearton: Methodology (equal); Writing – original draft (equal); Writing – review & editing (equal).

DATA AVAILABILITY

The data that support the findings of this study are available within the article.

REFERENCES

- ¹A. C. Twitchett, R. E. Dunin-Borkowski, R. J. Hallifax, R. F. Broom, and P. A. Midgley, J. Microsc. (Oxford, U.K.) **214**, 287 (2004).
- ²N. I. Kato, J. Electron. Microsc. **53**, 451 (2004).
- ³O. Wilhelm, S. Reyntjens, B. Van Leer, P. A. Anzalone, and L. A. Giannuzzi, Focused Ion, and Electron Beam Techniques, Handbook of Silicon Based MEMS Materials and Technologies, Micro and Nano Technologies (Elsevier, Amsterdam, 2010).
- ⁴J. Yan and N. Takayama, *Micro and Nanoscale Laser Processing of Hard Brittle Materials* (Elsevier, Amsterdam, 2020).
- ⁵D. Cooper, C. Ailliot, J.-P. Barnesa, J.-M. Hartmann, and P. Salles, Ultramicroscopy **110**, 383 (2010).
- ⁶M. H. Wong and M. Higashiwaki, IEEE Trans. Electron. Devices **67**, 3925 (2020).
- ⁷A. J. Green *et al.*, APL Mater. **10**, 029201 (2022).
- ⁸S. J. Pearton, F. Ren, M. Tadjer, and J. Kim, J. Appl. Phys. **124**, 220901 (2018).
- ⁹E. Ahmadi and Y. Oshima, J. Appl. Phys. 126, 160901 (2019).

- ¹⁰M. Higashiwaki, AAPPS Bull. 32, 3 (2022).
- ¹¹D. Kalanov, A. Anders, and C. Bundesmann, J. Vac. Sci. Technol. A 39, 053409 (2021).
- ¹²A. Nikolskaya et al., J. Vac. Sci. Technol. A **39**, 030802 (2021).
- ¹³K. Sasaki, M. Higashiwaki, A. Kuramata, T. Masui, and S. Yamakoshi, Appl. Phys. Express 6, 086502 (2013).
- ¹⁴R. Sharma, M. E. Law, C. Fares, M. Tadjer, F. Ren, A. Kuramata, and S. J. Pearton, AIP Adv. 9, 085111 (2019).
- 15 M. J. Tadjer et al., ECS J. Solid State Sci. Technol. 8, Q3133 (2019).
- ¹⁶R. Sharma et al., J. Vac. Sci. Technol. B 37, 051204 (2019).
- ¹⁷M. H. Wong, C. H. Lin, A. Kuramata, S. Yamakoshi, H. Murakami, Y. Kumagai, and M. Higashiwaki, Appl. Phys. Lett. 113, 102103 (2018).
- ¹⁸K. Tetzner, A. Thies, E. Bahat Treidel, F. Brunner, G. Wagner, and J. Würfl, Appl. Phys. Lett. 113, 172104 (2018).
- ¹⁹S. Luan, L. Dong, X. Ma, and R. Jia, J. Alloys Compd. **812**, 152026 (2020).
- ²⁰A. Azarov, C. Bazioti, V. Venkatachalapathy, P. Vajeeston, E. Monakhov, and A. Kuznetsov, Phys. Rev. Lett. **28**, 015704 (2022).
- ²¹ A. I. Titov, K. V. Karabeshkin, A. I. Struchkov, V. I. Nikolaev, A. Azarov, D. S. Gogova, and P. A. Karaseov, Vacuum 200, 111005 (2022).
- ²²J. Ziegler, J. P. Biersack, and M. D. Ziegler, SRIM—The Stopping and Ranges of Ions in Solids (SRIM Co., Chester, 2008), see www.srim.org.
- ²³J. F. Ziegler, J. P. Biersack, and U. Littmark, in *The Stopping and Range of Ions in Solids, The Stopping and Range of Ions in Matter*, edited by J. F. Ziegler (Pergamon, New York, 1985), Vol. 1.
- ²⁴J. P. Biersack and L. G. Haggmark, Nucl. Instrum. Methods 174, 257 (1980).
- ²⁵W. D. Wilson and L. G. Haggmark, Phys. Rev. B **15**, 2458 (1977).
- ²⁶W. Möller and W. Eckstein, Nucl. Instrum. Methods Phys. Res. 2, 814 (1984).
- ²⁷W. Möller, W. Eckstein, and J. P. Biersack, Comput. Phys. Commun. 51, 355 (1988).
- ²⁸A. Mutzke, R. Schneider, W. Eckstein, and R. Dohmen, "MPI for plasma physics," IPP Report 12/8, 2011.
- physics," IPP Report 12/8, 2011. ²⁹H. Hofsäss, K. Zhang, and A. Mutzke, Appl. Surf. Sci. **310**, 134 (2014).
- ³⁰S. J. Pearton, U. K. Chakrabarti, A. P. Perley, and K. S. Jones, J. Appl. Phys. 68, 2760 (1990).
- ³¹S. J. Pearton, C. R. Abernathy, F. Ren, and J. R. Lothian, J. Appl. Phys. 76, 1210 (1994).
- 32D. J. Werder and S. J. Pearton, J. Appl. Phys. 62, 318 (1987).
- ³³W. A. Grant and J. S. Williams, Sci. Prog. 63, 27 (1976), available at https://www.jstor.org/stable/43420342.
- ³⁴H. Sheoran, V. Kumar, and R. Singh, ACS Appl. Electron. Mater. 4, 2589 (2022).
- 35 S. Mukhopadhyay, L. A. M. Lyle, H. Pal, K. K. Das, L. M. Porter, and B. Sarkar, J. Appl. Phys 131, 025702 (2022).
- ³⁶L. A. M. Lyle, K. Jiang, E. V. Favela, K. Das, A. Popp, Z. Galazka, G. Wagner, and L. M. Porter, J. Vac. Sci. Technol. A 39, 033202 (2021).
- ³⁷J. Kim, S. J. Pearton, C. Fares, J. Yang, F. Ren, S. Kim, and A. Y. Polyakov, J. Mater. Chem. C 7, 10 (2019).
- 38S. J. Pearton et al., ECS J. Solid State Sci. Technol. 10, 055008 (2021).
- ³⁹Z. Islam, A. L. Paoletta, A. M. Monterrosa, J. D. Schuler, T. J. Rupert, K. Hattar, N. Glavin, and A. Haque, Microelectron. Reliab. 102, 113493 (2019).